A Data Fusion Approach to Optimize Compositional Stability of Halide Perovskites

Shijing Sun[1†]*, Armi Tiihonen[1†], Felipe Oviedo[1], Zhe Liu[1], Janak Thapa[1], Yicheng Zhao[2, 2a], Noor Titan P. Hartono[1], Anuj Goyal[3], Thomas Heumueller[2, 2a], Clio Batali[1], Alex Encinas[1], Jason J. Yoo[1], Ruipeng Li[4], Zekun Ren[5], I. Marius Peters[2], Christoph J. Brabec[2, 2a], Moungi G. Bawendi[1], Vladan Stevanovic[3], John Fisher III[1], Tonio Buonassisi[1,5*‡]

[1]Massachusetts Institute of Technology, Cambridge, MA 02139, USA

[2]Helmholtz-Institute Erlangen-Nürnberg (HI-ERN), Erlangen, 91058, Germany

[2a]Institute of Materials for Electronics and Energy Technology (i-MEET), Friedrich-Alexander-Universität Erlangen-Nürnberg (FAU), Erlangen, 91058, Germany

[3]Colorado School of Mines, Golden, CO 80401, USA

[4]Brookhaven National Laboratory, Upton, NY 11970, USA

[5]Singapore-MIT Alliance for Research and Technology, 138602, Singapore

[†]These authors contributed equally.

*Correspondence to: shijings@mit.edu, buonassisi@mit.edu

[‡]Lead Contact: Tonio Buonassisi

Summary

Resource-efficient materials search in vast compositional spaces is an outstanding challenge in creating environmentally stable perovskite semiconductors. We demonstrate a physics-constrained sequential learning framework to subsequently identify the most stable alloyed organic-inorganic perovskites. We fuse data from high-throughput degradation tests and first-principle calculations of phase thermodynamics into an end-to-end Bayesian optimisation algorithm using probabilistic constraints. By sampling just 1.8% of the discretized $Cs_xMA_yFA_{1-x-y}PbI_3$ (MA=methylammonium, FA=formamidinium) compositional space, perovskites centred at $Cs_{0.17}MA_{0.03}FA_{0.80}PbI_3$ show minimal optical change under elevated temperature, moisture, and illumination with >17× stability improvement from $MAPbI_3$. The thin-films have 3× improved stability compared to state-of-the-art multi-halide $Cs_{0.05}(MA_{0.17}FA_{0.83})_{0.95}Pb(I_{0.83}Br_{0.17})_3$, translating into enhanced solar cell stability without compromising conversion efficiency. Synchrotron-based X-ray scattering validates the suppression of chemical decomposition and minority phase formation achieved using fewer elements and maximum 8% MA. We anticipate that this data fusion approach can be extended to guide materials discovery for a wide range of multinary systems.

Introduction

The environmental instability of organic-inorganic halide perovskite materials limits their usage in optoelectronics such as solar cells, light emitters, lasers, and photodetectors.[1] Compositional engineering is to date one of the most effective methods to improve perovskites' stability in the presence of heat, humidity and light without sacrificing optoelectronic performance.[2] This fact has led to intensive research within combinatorial spaces such as $A_xB_yC_{1-x-y}Pb(I_zBr_{1-z})_3$.[3] However, only a small fraction of this compositional space has been experimentally explored, in part due to the prohibitively expensive brute force synthesis. The paucity of resulting degradation data inhibits generalisation of mechanisms across this diverse chemical and structural space, requiring each compositional search to start their experimental investigations *ab initio*.[4] This challenge is similar to those faced by other materials communities, including heterogeneous catalysts, alloyed battery electrodes, and high-entropy metal alloys for structural and magnetic materials.[5–7] The halide perovskite field and several others require new tools to experimentally navigate these vast spaces efficiently to locate optima and to extract generalisable scientific insights.[8–14]

Machine-learning-based sequential learning approaches (e.g. Bayesian optimisation, BO) have emerged as efficient materials search tools that explore vast variable spaces in a 'closed-loop' fashion, whereby the outcome of one experimental round informs the next without human intervention. BO has attracted increasing attention in the recent developments of self-driving laboratories in various fields of materials science, recently successfully directed experimentation in the search of organic hole-transport materials[15], piezoelectric oxides,[16] and organic photocatalysts.[10] Within the field of perovskite solar cells, machine-learning has been combined with robotic liquid synthesis for microcrystal crystallization.[17–20] However, such model-free statistical approach show limitations without principled guidance from domain expertise, because it has to learn everything from scratch. Recent *in situ* experiments and first-principle calculations independently reveal insights into the fundamental composition-dependent instability in organic-inorganic perovskites and their alloys, however, merging computational and experimental insights on selective compositions into a generalisable optimisation policy over the entire chemical space remains a challenge.[3] State-of-the-art two-step approaches of directly applying theoretical screening as a hard constraint prior to shortlisted synthesis are limited by the inefficiencies from:

1) high-performing theoretical calculations for organic–inorganic systems are often too sparse to guide experimentation, and 2) the discrepancies between the calculation assumptions and the experiments at non-thermodynamic equilibria decreases search accuracy.[21,22] The lack of physics-informed and iterative materials search hinders the ultimate goal of designing perovskite compositions for enhanced environmental stability.

Here we introduce a data fusion approach to incorporate both Gibbs free energy of mixing (ΔG_{mix}) from density functional theory (DFT) calculations[23] and experimentally quantified degradation from accelerated aging tests to every decision that the BO algorithm is making. We apply this closed-loop machine-learning framework to optimise lead-iodide perovskites that suffer from severe heat and moisture-induced degradation within the five-element space of $Cs_xMA_yFA_{1-x-y}PbI_3$. Under multiplex environmental stress tests with elevated temperature, humidity, and illumination in air, we identify compositions overperforming the $MAPbI_3$ starting-point by 17× and our state-of-the-art reference composition of $(Cs_{0.05}(MA_{0.17}FA_{0.83})_{0.95}Pb(I_{0.83}Br_{0.17})_3)$ by 3× within three optimisation rounds, and the results are found transferable to device stability. DFT here serves as principled guidance within the decision-making algorithm to constrain the search space to not only chemically, but also the structurally stable α-perovskite alloys.

Results and Discussion

Closed-loop Experimentation Platform Driven by Physics-informed Bayesian Optimisation

To efficiently guide the compositional search, we construct a physics-informed batch Bayesian optimisation (BO) framework (Figure 1). In BO, promising compositions for the next experimental round are suggested by an acquisition function, such as *expected improvement* $EI(\Theta)$ that balances the exploitation of the most stable regions and the exploration of high-uncertainty regions within the compositional space. As a key algorithm contribution, we fuse ΔG_{mix} as a *probabilistic constraint* of the BO acquisition function in the 'composition selection' step, providing additional information on phase stability to effectively identify multi-cation perovskites that are thermodynamically stable relative to their single-cation counterparts (Figure 1a-b). We define '*Instability Index' (I_c),* a figure of merit for optimising stability. The goal of each optimisation

round, which consists of three steps of 'composition selection', 'film synthesis' and 'instability quantification', is to minimise this value. Our batch BO algorithm makes use of a surrogate ML model, Gaussian process regression (GP),[24] to estimate the value and uncertainty of I_c in non-explored regions of the compositional space (see Experimental Procedures).

Within each optimisation round (one batch in BO), 28 spin-coated thin-film samples (Figure 1c) are examined *in situ* in parallel using an environmental chamber under 85 RH% and 85°C in the air (Figure S1). 0.15 Sun visible only illumination is applied to enable automatic image capture every five minutes by an RGB camera (~200 μm resolution). Photoactive α-perovskite phases within $Cs_xMA_yFA_{1-x-y}PbI_3$ exhibit a bandgap of ~1.5 eV, whereas their main degradation products under hot and humid conditions, PbI_2 (2.27 eV),[25] δ-$CsPbI_3$ (2.82 eV)[26] or δ-$FAPbI_3$ (2.43 eV)[27] show deteriorated photophysical properties (Figure S2). As per Figure 1d, we hence employ a colour-based metric as a proxy to capture the macroscopic evolution of the high-bandgap, non-perovskite phases.[28–30] We define *Instability Index (I_c)* as the integrated colour change of an unencapsulated perovskite film over accelerated degradation test duration *T*. Complementary direct bandgap measurements before and after the degradation tests via UV-Visible spectroscopy are listed in Figure S12.

$$I_c\,(\Theta) = \sum_{c=\{R,G,B\}} \int_{0min}^{T} |c(t,\Theta) - c(0,\Theta)|\, dt, \quad (1)$$

where composition $\Theta = (x, y, 1-x-y)$, *t* is time, and *c* are area-averaged, colour-calibrated red, green and blue pixel values of the sample. The cut-off time was set to T=7000min based on the observed divergence between the most and least stable compositions (Figure S3). Our closed-loop and iterative workflow enable the systematic optimisation of multi-cation perovskites against degradation by varying the nominal compositions, Θ, within $Cs_xMA_yFA_{1-x-y}PbI_3$ (x, y limit to two decimal places) (Table S1-2).

Data fusion Approach: Incorporation of Phase Thermodynamics into Automated Composition Selection

Due to their polymorphic nature, identical perovskite compositions crystallised into different phases can exhibit diverse degradation behaviours, making it essential to evaluate phase stabilities in any perovskite composition optimisation.[1] The end members of the compositional space in

this study consist of the cubic α-FA/MAPbI$_3$ perovskites and the non-perovskite δ-CsPbI$_3$ at the synthesis temperature.[31]. Phase de-mixing during synthesis leads to minority phases within thin-film samples prior to degradation tests and are, therefore, not captured in I_c. Nevertheless, phase de-mixing during film formation or soon after is not desirable because it deteriorates the electronic properties of the perovskite.[32] Schelhas *et al.* recently demonstrated the use of DFT calculations to predict the phase de-mixing tendency between α-Cs$_x$MA$_y$A$_{1-x-y}$PbI$_3$ (G_{mix}) and their single-cation perovskite polymorphs *A*PbI$_3$ (*A* = Cs, MA, or FA) (G_0) at a given temperature.[23] We herein fuse the composition-dependent change in Gibbs free energy of mixing, ΔG_{mix} as a constraint into the experimental optimisation loop (Figure 2a). This approach allows the α- and δ-phase relative stability in the non-degraded perovskite samples to be considered in the composition selection, thus enabling us to reduce sampling in regions with high probability of minority phase formation.

Data fusion refers to a set of techniques where ML is used to map two or more datasets coming from related but distinct distributions. In our case, we relate the theoretical $\Delta G_{mix}(\Theta)$ and the experimental $I_c\,(\Theta)$. The two data streams account for distinct mechanisms of modelled thermodynamic phase instability and measured macroscopic thermal-moisture instability, respectively. Hence, it is inadequate to combine both datasets as equivalent or include DFT directly as a prior following state-of-the-art model-free BO.[33,34] We herein define a data-fused *probabilistic constraint* approach according to Eq. (2):

$$P(\Delta G_{mix}(\Theta), \beta_{DFT}) = \frac{1}{1 + e^{-\Delta G_{mix}(\Theta)/\beta_{DFT}}}, \qquad (2)$$

where $P(\Delta G_{mix}(\Theta), \beta_{DFT})$ is a logistic cumulative distribution function (CDF) modelling the phase mixing probability and β_{DFT} is a data fusion parameter calibrated according to ΔG_{mix} calculations to control the smoothness of the boundaries from stable to unstable compositions, forming a soft compositional boundary presented in Figure 2a (see Experimental Procedures for algorithm details).

Given the computational cost and complexity of DFT calculations on organic-inorganic hybrid systems, we first regress 85 DFT-modelled ΔG_{mix} values on 47 single-cation and binary alloyed compositions (29 MAFA and CsFA compositions from Schelhas *et al.*[23] 12 CsMA compositions computed for the present work using the same methods) over the quasi-ternary Cs$_x$MA$_y$A$_{1-x-y}$PbI$_3$

phase space using an auxiliary GP model that defines $\Delta G_{mix}(\Theta)$. Figure 2a visualises the probability of phase mixing $P(\Delta G_{mix}(\Theta), \beta_{DFT}) \in [0,1]$, where low values suggest phase instability ($\Delta G_{mix} >> 0$) and high values suggest phase stability ($\Delta G_{mix} << 0$).

Our work is inspired by the *unknown constraint* BO proposed by Gelbart *et al*.[35] By developing a probabilistic constraint model $P(\Delta G_{mix}(\Theta), \beta_{DFT})$ instead of applying a hard-constraint boundary, we are able to discount regions predicted by DFT to go through phase demixing rather than completely exclude any unfavourable regions. This approach accounts for the inherent uncertainty in DFT predictions, chemical accuracy, and data scarcity through the use of the soft compositional boundary to model the stability threshold (see Experimental Procedures for β_{DFT} calibration). The proposed algorithm allows us to seamlessly adapt DFT into the experimental optimisations loop, thereby achieving a physics-informed and sample-efficient search without being limited by the unknown exact phase boundaries across a vast compositional space (Figure S4-5).

To integrate the *probabilistic constraint* into the BO formulation, we weigh the acquisition function with the value of $P(\Delta G_{mix}(\Theta), \beta_{DFT})$ and obtain a DFT-weighted BO acquisition function, $EIC(\Theta)$, as illustrated in Figure 2a. Traditional $EI(\Theta)$ utilizes the I_c results of our first experimental round without DFT and indicates two potential optima in Cs-poor and Cs-rich regions, respectively. The DFT-weighted $EIC(\Theta)$ effectively reduces sampling in energetically unfavourable Cs-rich regions despite low I_c: the subsequent optimisation rounds converge to stable nominal compositions with a high probability of stable α-perovskite films among Cs-poor regions (Figure 2a, Figure S6-7). Comparisons of optimisation with and without DFT-weighting using a teacher-student model are shown in Figure S8-9, which validates that without data fusion, the model-free BO algorithm continues to suggest sampling in Cs-rich regions despite of their phase instability.

Figure 2b demonstrates that batch BO sequentially identifies the most stable regions over one initialization and three optimisation rounds of synthesis and degradation tests. Iterative evolution of the landscape (posterior mean of I_c, $I_c(\Theta)$, with uncertainty) is presented in Figure S3-S4. Figure 2c reveals a rapid decrease in experimentally quantified I_c from Rounds 0–3. The search converges after three optimisation rounds (see Figure S5 for convergence conditions) to an optimal composition region centred at $Cs_{0.17}MA_{0.03}FA_{0.80}PbI_3$ and bounded by 8-29% Cs, <14 % MA and

68-92 % FA. The identification of the global optimum lying within an FA-rich, Cs and MA-poor region is consistent with the reports that FA-rich perovskites show superior environmental stability compared with their MA-rich counterparts and the less volatile Cs is expected to enhance the heat and moisture resistance.[36] Interestingly, we found a local optimum near $Cs_{0.26}MA_{0.36}FA_{0.38}PbI_3$, which emerged in Round 1. We sample four additional compositions in Round 3 and validate that the non-intuitive local optima suggested by the algorithm is reproducible. The ability to rapidly identify non-intuitive regions of success is a major advantage of using an automated closed-loop optimization algorithm over materials search strategies leveraging the human intuition alone. Further experimental validation and mechanisms study of the identified compositional regions of interest are discussed in the next sub-section. We define the compositional space as the discretized quasi-ternary phase space subdivided by the minimum achievable experimental resolution (1% composition). This yields 5151 possible singular, binary and ternary cation compositions, 1.8% of which were sampled experimentally while converging to the optimal region (i.e., 94 unique compositions and 112 samples within Round 0 – Round 3, see supplementary information for more details). Three additional degradation rounds of seven representative compositions were performed, to validate the instability trend with structural and optical characterisation shown in the Table S3, Figure S10-13.

Composition-, Phase-, and Time-dependent Instability Landscapes

We find the overall stability landscape within the $Cs_xMA_yFA_{1-x-y}PbI_3$ compositional space to be non-linear. To quantify the divergence in degradation profiles, Figure3a presents the composition-dependent instability landscape, $I_c(\Theta)$ for $Cs_xMA_yFA_{1-x-y}PbI_3$ after three experimental optimisation rounds, where three distinct compositional regions (Region III ->I) with descending I_c are clearly identified. The evolution of $I_c(\Theta)$ as a function of degradation time, as per Figure S3, further reveals that fast degradations of MA-rich compositions are evident after six hours of degradation tests (Region III), while two additional regions, representing compositions in local optima (Region II) and the global optima (Region I), are sequentially distinctive after 100 hours of degradation tests. Experimentally measured I_c data reveals a > 17× reduction from the $MAPbI_3$ end-point in Region III to the ML-optimum, at $Cs_{0.17}MA_{0.03}FA_{0.80}PbI_3$, in Region I. Interestingly, several MA-containing compositions show comparable I_c to their CsFA binary cation counterparts

as per Figure 3b. Up to 8% MA, the least chemically stable cation in the design space, can be added into the perovskite structure before environmental stability is significantly compromised.

Figure 3b visualises experimentally measured I_c as a function of Goldschmidt's tolerance factor (TF) calculated using the average ionic radius of A-site cations in nominal compositions. TF is empirical guidance that has been widely applied to estimate the intrinsic structural stability of hybrid perovskites.[37,38] We find that TF optimisation is necessary but not sufficient criteria for achieving high environmental stability. During optimisation Rounds 1–3, an increasing number of compositions within a TF of 0.93–0.97 are suggested by ML, indicating high stability of compositions with a TF of around 0.95. This value is lower than TF = 1 of an ideal cubic structure, attributing to the incorporation of small-radius and non-volatile Cs into the α-lattice to improve moisture and heat resistance (Figure S11).

To validate the scientific relevance of the data fusion approach, which effectively discounts experimental sampling in the regions with high probabilities of minority phase formation, we seek to determine the impact of thermodynamics-driven minority phases on degradation dynamics. Within the $Cs_xMA_yFA_{1-x-y}PbI_3$, we examine the structural evolution after 0, 6- and 100-hours' degradation tests respectively using *ex situ* synchrotron-based grazing-incidence wide-angle scattering (GIWAXS) measurements (Figure S14-15). Comparing the ML-local optimum, (ii) $Cs_{0.26}MA_{0.36}FA_{0.38}PbI_3$ in Region II, and the ML-optimum, (i) $Cs_{0.17}MA_{0.03}FA_{0.80}PbI_3$ in Region I (Figure 4a), we observe that the two compositions (i) and (ii) exhibit comparable lattice parameters of α-perovskites, however, local optimum (ii) contains additional δ-$CsPbI_3$ minority phase prior to degradation tests. Interestingly, only a slightly larger increase in PbI_2 is observed in (ii) than in global optimum (i) after a 6-hour degradation run. After 100 hours, (ii) exhibits a significantly bigger loss of intensity of α-perovskites and crystallinity (Figure S14).

To understand the distinctive roles of MA, Cs, and minority phases that governs the divergence in degradation profiles behind the optimisation results, we further quantify the peak intensities of PbI_2 (001), δ-$CsPbI_3$ (002), $FAPbI_3$ (001) and α-perovskite (001) of four representative compositions in Region I and II (Figure 4c-f). Two composition-dependent degradation mechanisms are observed (Figure S16-17, Table S5-6). While all four samples show increased PbI_2 content (evident of chemical decomposition to precursors), the emergence of δ-$CsPbI_3$ and δ-$FAPbI_3$ minority phases in Region I films with low Cs- and MA-content (Figure 4e and f) indicates

additional mechanisms of phase separation during degradation tests. We find MA plays a competing role as it accelerates chemical decomposition while suppresses phase separation (additional X-ray diffraction results shown in Figure S10). Reducing MA content from 8% to 3% (Figure 4e and f) show effective suppression of chemical decomposition within the first 6 hours. If we remove MA completely, we observe a faster phase separation emerged between 6 -and 100 hours of degradation (Figure 4c and d). Phase separation as a degradation mechanism is observed to take place in a longer time scale compared with chemical decomposition. Overall, the stability optimisation pathway from Region II to Region I in order to achieve kinetically suppressed degradation can be summarized as follows: 1) reducing MA to suppress chemical decomposition, 2) reducing Cs to limit thermodynamics-driven minority phase formation, and 3) balancing MA, FA, and Cs for restraining additional minority phase formation in hot and humid conditions.

Insights into the Effects of Compositional Complexity on Thin-film and Device Stability

To determine the impact of ML-informed compositions in the field of perovskite optoelectronics, we first demonstrate the thin-film stability improvement in this study against the state-of-the-art. Figure 5a illustrates the quantitative optical change analysis for three representative thin-film compositions from Region I, including the ML-optimum $Cs_{0.17}MA_{0.03}FA_{0.80}PbI_3$ (i), the ML-local optimum $Cs_{0.26}MA_{0.36}FA_{0.38}PbI_3$ (ii), and $MAPbI_3$ (iii). We further compare the optimised five-element iodide perovskites (i) with a six-element iodide-bromide reference composition, $Cs_{0.05}(MA_{0.17}FA_{0.83})_{0.95}Pb(I_{0.83}Br_{0.17})_3$ (iv) (I/Br). I/Br is outside the design space of this study (referred to as Region IV), but is among the most widely employed compositions in high-efficiency perovskite solar devices.[36,39,40] We found that (i) yields a 3.5x lower I_c than (iv). In addition to suppressed total degradation in optimized iodide perovskites, the degradation onset is also postponed. This is reflected by the > 3× delay in the onset of sharp optical change as per Figure 5a. The ML-optimum within the iodide perovskite space overperforms the more complex iodide-bromide mix, which contradicts a long-standing assumption in the perovskite field that increasing compositional complexity entropically stabilizes the absorber. The overall environmental stability based on thin-film stability is Region I > Region II > Region IV > Region III.

We then demonstrate the enhanced stability of full photovoltaic devices without compromising conversion efficiency. To ensure rigorous environmental tests that matches the reliability requirement for perovskite solar cell commercialization, we employ air ambient, 85% relative

humidity, and 85°C temperature full damp heat testing on non-encapsulated devices (close to the conditions of accelerated film degradation tests), which is a much harsher stress condition than most of current laboratory testing for perovskite devices. Figure 5b reveals that devices of the three ML-informed compositions from Region I all overperform the state-of-the-art I/Br reference, leading to an increased efficiency (post-aging/prior-to-aging) ratio from 73% to 87% after 50 hours accelerated degradation test. While devices of both the ML-optimum and the reference composition show initial efficiencies of >19% (as per Figure 5c and d), more severe photocurrent decay is observed in the reference. An average of the 77% of the performance is maintained in the ML-optimum in comparison to 71% in I/Br (Figure 5b, over 18 devices) after degradation tests. In addition to the ML optimum (3% MA), two other Region I iodide perovskites, $Cs_{0.13}MA_{0.08}FA_{0.79}PbI_3$ (8% MA) and $Cs_{0.13}FA_{0.87}PbI_3$ (0% MA) also overperform I/Br in both film and device stability (Figure S18). We find that compositions with fewer elements lead to improved thermo-moisture stability, where the MA-free, iodide-only composition in this comparative study achieved the highest device stability.

We should note that in a solar cell, other layers rather than the absorber within a device may also accelerate the degradation depending on the device architectures. Non-encapsulated full devices are often found to undergo faster degradations than bare films, in particular in the first several hours, attributing to interface-related degradations.[4,23] In this study we only focus on the correlations between film and device stability from an angle of perovskite layer degradation without device architecture optimisation. To confirm if the device stability improvement holds under additional stress of 1Sun illumination, we further compare the photostability of devices under 1Sun at 65°C in N_2, (different from the conditions applied for thin-film optimisation in this study) and the results show a photo-thermostability of 8% MA > ML-optimum (3% MA) > I/Br > 0% MA (Figure S19). The higher device photostability of MA-containing compositions suggest a beneficial role of MA in suppressing illumination-induced degradation in multi-cation iodide perovskites.

Our device stability results highlight the non-intuitive conclusion that simplifying the perovskite formulation yields a higher device stability in hot and humid environments. This finding emphasizes the importance of achieving a holistic understanding of a compositional space to effectively identify optima. The physics-constrained sequential learning approach developed in

this study can be extended to experimentally navigate higher-dimensional spaces under operational conditions, such as to identify the most environmental stable iodide-bromide-chloride perovskite alloys in the growing chemical space of $A_xB_yC_zD_{1-x-y-z}Pb(I_pBr_qCl_{1-p-q})_3$, in order to further improve perovskite solar cells' efficiency and reliability.

Conclusions

In this study we develop a closed-loop optimisation strategy for $Cs_xMA_yFA_{1-x-y}PbI_3$ multi-cation perovskites against heat, moisture and light-induced degradation by introducing a physics-constrained Bayesian optimisation framework. We identify an FA-rich and Cs-poor region centred at $Cs_{0.17}MA_{0.03}FA_{0.8}PbI_3$ with > 17× stability optimisation from $MAPbI_3$ while sampling only 1.8% of the discretized compositional space, achieving superior search efficiency and scientific relevance to brute-force screening and state-of-the-art model-free Bayesian optimisation, respectively. The study demonstrates the power of data fusion to allow material search over vast and sparsely-sampled compositional spaces, where the DFT-modelled phase mixing serves as a *probabilistic constraint* and provides principled guidance to ML-directed experimentation.

We apply this physics-informed optimisation framework to achieve a holistic understanding of the fundamental composition-, phase-, and time-dependent behaviour of organic-inorganic perovskites. As a consequence of competing roles of cations in different degradation mechanisms, a composition window of up to 8% addition of the least chemically stable cation, MA, contributes to kinetically suppressed degradation, whereas the most chemically stable cation in this design space, Cs, contributes to accelerated degradation through phase separation even in the most macroscopically-stable candidates found in the $Cs_xMA_yFA_{1-x-y}PbI_3$ compositional space, which potentially limits the benefits of Cs as a perovskite stabilizing agent. These findings highlight the detrimental effects of minority phase formation as a degradation pathway, which occurs over a longer timeframe than chemical decomposition, and hence are easily underestimated in the initial compositional engineering. We further suggest several optimized iodide perovskites, including $Cs_{0.17}MA_{0.03}FA_{0.8}PbI_3$, and $Cs_{0.13}MA_{0.08}FA_{0.79}PbI_3$ that show superior photo-, thermo-, and moisture device stability to the state-of-the-art iodide-bromide mixed perovskite ($Cs_{0.05}(MA_{0.17}FA_{0.83})_{0.95}Pb(I_{0.83}Br_{0.17})_3$), providing insights into simplifying perovskite compositions for solar cell reliability.

This data fusion approach combines multiple data sources into a single search algorithm and can be utilised to include other experimental or theoretical constraints with non-negligible uncertainty into the materials design strategy. The method can be generalized to direct experimentation in other material systems, merging complementary experiments and theory to collectively inform synthesis in a closed-loop fashion across a vast chemical and structural space.

Experimental Procedures

Resource Availability:

Lead Contact: Further information and requests for resources and reagents should be directed to and will be fulfilled by the Lead Contact, Tonio Buonassisi (buonassisi@mit.edu).

Materials Availability: This study did not generate new reagents. Reagents used were purchased from Sigma-Aldrich as described in subsection Materials.

Data and Code Availability: Details of materials, experimental methods, machine learning framework and camera-based *in situ* degradation monitoring platform details are available in Supplemental information. The codes and the datasets used for Bayesian optimisation are available in GitHub repository https://github.com/PV-Lab/SPProC. Lists of samples and raw data of XRD characterization, and thin-film degradation results are shown in Supplemental Data.

Materials: Perovskite precursor solutions were spin-coated on UV-ozone glass substrates. Glass microscope slides (VWR) cut into square pieces were cleaned with sonication in 2% Hellmanex-DI water mix, DI water, and IPA respectively. We perform perovskite synthesis with over-stoichiometric PbI_2 in the molar ratio of 1.09 (PbI_2) to 1 (halide salt of CsI, MAI, and FAI). Lead (II) iodide stock solution was prepared in 9:1 N,N-dimethylformamide (Sigma-Aldrich) to dimethyl sulfoxide (Sigma-Aldrich) solvent. The perovskite precursor solution was prepared by mixing individual stock solutions following the ratios of Cs, FA, and MA suggested by the machine learning algorithm. The films were annealed at 403 K for 20 minutes using the central part of a hot plate in the glovebox. The spin-coating program follows a 2-step approach: 1000 rpm for 10 seconds and acceleration of 200 rpm/s, with a subsequent 6000 rpm for 30 seconds and acceleration of 2000 rpm/s. Chlorobenzene (Sigma-Aldrich) antisolvent in the quantity of 150 μL

was dropped 5 seconds at the beginning of the second step of spin-coating. The annealed samples were cooled to room temperature before transferring to the degradation test. $Cs_{0.05}(FA_{0.83}MA_{0.17})_{0.95}Pb(I_{0.87}Br_{0.13})_3$ was synthesized following Ref. [41].

Aceelerated degradation tests: Humidity, temperature, and visible light illumination level were controlled at 85±2°C, 85±5%, and 0.15±0.01Sun, respectively, using an in-house built environmental chamber. Samples were photographed automatically in every 5 min during the aging test, and additionally the humidity and temperature of the aging chamber were tracked automatically. The illumination conditions remaining stable during the aging tests was confirmed by following a reference colour chart that had been placed into the picture area and the collected data was color-calibrated (see Supplemental Methods). Accelerated degradatation, automation, parallel degradation of 28 samples, and fault-resistant measurement method via photographing enabled high-throughput aging testing compared to traditional methods. After the aging test, the samples were stored in a glovebox until further characterization.

Physics-informed BO framework: In the Bayesian optimisation setting, a surrogate machine learning model, Gaussian Process (GP) regression, is used to approximate the mean and uncertainty of $I_c(\Theta)$ in non-sampled regions of the compositional space. Once the model is fitted, an *acquisition function* is used for suggesting locations in the compositional space with high chance of leading to an optimum. Our chosen base acquisition function that we modify by data fusion principle is *expected improvement* $\mathrm{EI}(\Theta)$,

$$\mathrm{EI}(\Theta) = (\mu_n(\Theta) - \tau)\Phi\left(\frac{\mu_n(\Theta) - \tau}{\sigma_n(\Theta)}\right) + \sigma_n(\Theta)\,\phi\left(\frac{\mu_n(\Theta) - \tau}{\sigma_n(\Theta)}\right)$$

where Φ is the standard normal cumulative distribution, $\mu_n(\Theta)$ is the mean of the surrogate model's (here Gaussian process regression, GP) posterior, τ is an incumbent best point, σ_n is the variance of the GP model's posterior, ϕ is the standard normal probability distribution, and n is degradation round. By maximizing $\mathrm{EI}(\Theta)$, the most promising location Θ^* (either due to a low expected instability index or a high uncertainty of the estimate) for the next experimental round is determined. To suggest more than the one promising composition Θ per round, we employ the local penalization algorithm to resample $\mathrm{EI}(\Theta)$, as described in [42]. To include the physical

constraints in the Bayesian optimisation algorithm, the acquisition function is weighted according to the probabilistic model $P(\Delta G_{\mathrm{mix}}(\Theta), \beta_{\mathrm{DFT}})$ following the method in ref.[35]:

$$\mathrm{EIC}(\Theta) = \mathrm{EI}(\Theta)\, P(\Delta G_{\mathrm{mix}}(\Theta), \beta_{\mathrm{DFT}})$$

Once ΔG_{mix} is modelled (see Supplemental Methods), the probabilistic model $P(\Delta G_{\mathrm{mix}}(\Theta), \beta_{\mathrm{DFT}})$ can be computed. The inherent bias and precision of DFT calculations justifies the probabilistic treatment of the constraint. Referring to the constraint value as $\Phi = P(\Delta G_{\mathrm{mix}}(\Theta), \beta_{\mathrm{DFT}})$, we formulate the data fusion process as maximizing the likelihood $\mathcal{L}(\beta_{\mathrm{DFT}}; \Phi, \Delta G_{\mathrm{mix}})$ such that:

$$\beta^*_{\mathrm{DFT}} = \mathrm{argmax}_{\beta_{\mathrm{DFT}}} \mathcal{L}(\beta_{\mathrm{DFT}}; \Phi, \Delta G_{\mathrm{mix}})$$

Using a Bernoulli likelihood, this definition is equivalent to fitting a logistic regression model via maximum likelihood, with ΔG_{mix} as the independent variable and the probability of phase de-mixing as the dependent variable. In this sense, one could estimate a certain critical energy above which the crystalline structure is unstable and will decompose into its constituent phases. In the context of convex hull stability calculations, this value is often considered to be around -0.025 eV/f.u. We hence choose β_{DFT} so that it produces cumulative probability of $P(-0.025\mathrm{eV}/f.u, \beta^*_{\mathrm{DFT}})$=0.7 and $P(-0.05eV/f.u, \beta^*_{\mathrm{DFT}})$=0.9. This assumption defines a smooth gradual boundary for phase mixing in the compositional space, considering the inherent uncertainty of first-principles calculations. Our choice of probabilistic model is common in machine learning literature, due to the simplicity and expressivity of logistic models.[43]

DFT Calculations: The methodology used here for alloyed halide perovskites has been discussed in detail in our recently published work in Refs.[23,44]. In this paper we performed additional DFT calculations for the binary (Cs-MA) and ternary (Cs-MA-FA) alloys as well as employed our previously published DFT calculations on binaries (Cs-FA, FA-MA) from Ref.[23] to generate adequate initial DFT data in the three-dimension phase spacethat feeds into the optimization model. DFT calculations are performed within the projected augmented wave (PAW) method[45] as implemented in the VASP code.[46] The Perdew Burke Ernzerhof (PBE) exchange correlation functional[47] is used with GGA and spin-orbit coupling (SOC) is included in the total energy calculations. Plane wave cutoff of 340 eV, and a Monkhorst-Pack k-point sampling scheme[48] is used. Alloy structures are created using the pseudo-cubic as the starting structure for the pure compositions (obtained from Ref.[49]) with random substitution at the A-

site. Special quasi-random structure (SQS) method,[50] as implemented in the ATAT package,[51,52] is used to obtain structures for various A-site alloy compositions. Two different supercell sizes 96 and 144-atoms are used and for each A-site composition with multiple (two or three) structures, varying in the orientation of the MA and FA molecules, are considered. For both pure and alloy phase calculations all degrees of freedom (cell shape, volume, and ionic positions) are relaxed in DFT. Following the relaxations, A-site alloy structures at various compositions are found to retain the overall cubic symmetry. As benchmarked in Ref.[53], the reproducibility and precision in our DFT total energy calculations is very high.

Thermodynamic Modeling: To model the thermodynamic phase stability of mixed A-site halide perovskites, we compute the Gibbs free energy of mixing ($\Delta G_{mix} = \Delta H_{mix} - T\Delta S_{mix}$) of these materials as a function of the A-site composition. The modeled ΔG_{mix} has two components, (1) the enthalpy of mixing (ΔH_{mix}), and the entropy of mixing (ΔS_{mix}). The enthalpy of mixing is calculated from DFT by taking the difference between the total energy of the mixed A-site halide perovskite with respect to the total energy of the constituent, or pure, phase. The temperature dependence ($T\Delta S_{mix}$) to Gibbs free energy is incorporated by considering the entropic contributions associated with the configuration and rotations degrees of freedom.Further details of thermodynamic modeling can be found in the Ref.[23]. The variability in the computed value of Gibbs free energy at a specific composition is between 5 – 20 meV/unit, and it comes from the varying orientation of the FA and MA molecules between the multiple structures, considered in our simulations.

X-ray diffraction: Grazing incidence X-ray diffraction (incident angle of 1°) were performed using Rigaku SmartLab with Cu-*K*α sources on the as-synthesized thin films to understand the crystal structures and to examine minority phases.

UV-visible spectroscopy: The absorptance for the films was calculated based on transmission and reflection measurements done using Perkin-Elmer Lambda 950 UV/Vis Spectrophotometer (Perkin-Elmer). Bandgaps were calculated using Tauc methods assuming direct bandgaps.

Scanning electron microscopy: The film morphology was investigated using a ZEISS Ultra-55 field-emission scanning electron microscope (FESEM, ZEISS), with InLens detector and 3.00 kV EHT gun. The grain sizes were counted using ImageJ within the area of ~0.72 μm^2. Various compositions show different distribution of grain sizes. The grain sizes of composition with high

Cs ($Cs_{0.26}FA_{0.74}PbI_3$), with Cs > 20%, are mostly between 300-500 nm and some of them reach up to 1200 nm, indicating the presence of δ-phase. The grain sizes of $MAPbI_3$ are mostly between 200-400 nm, and reach up to 1000 nm. The grain sizes of the rest of the compositions, which have low Cs (< 20%) are mostly between 200-400 nm.

GIWAXS measurements: Grazing-incidence wide-angle x-ray scattering (GIWAXS) measurements were taken at beamline 11-BM (CMS) at the National Synchrotron Light Source II (NSLS-II) of Brookhaven National Laboratory. The x-ray beam with the energy of 13.5 keV shone on the perovskite films in the grazing incident geometry. The data presented in the study was taken at incident angle $\theta = 0.2$ which probes the bulk structure of the films. The scattering spectra were collected with the exposure time of 30 seconds by an area detector (DECTRIS Pilatus 800K) placed 257 mm away from the sample. The data analysis was performed by using custom-made software SciAnalysis.[54]

Device fabrication: Unless stated otherwise, all materials were purchased from Sigma Aldrich or Merck and used as received. MAI and FAI were purchased from Xi'an P-OLED. PbI_2 was purchased from Lumtec. The Ta-WO_x colloidal solution was purchased from Avantama Ltd. The SnO_2-PEIE solution was prepared by mixing 15 wt% SnO_2 aqueous solution (300 μL) with 1.8 mL of isopropanol and H_2O (1/1, v/v) and 20 μL of PEIE. First, ITO substrates were sonicated in acetone/isopropanol for 10 minutes/5 minutes, respectively. Before spin coating SnO_2-PEIE solution (80 μL) at 3500 rpm for 30 seconds, the ITO substrates were treated by UV-Ozone for 10 minutes in ambient air. After annealling at 150°C/10 minutes in ambient air, 80 μL of PCBM:PMMA solution was spin-coated on a SnO_2/PEIE layer at 2000 rpm for 30 seconds and then annealed at 150°C for 10 minute. 1.2 M PbI_2 and FAI solution was prepared first in DMF and DMSO (4:1 v/v), and 1.2 M MAI/CsI solution was prepared in DMSO. The $MA_xCs_yFA_{1-x-y}PbI_3$ precursors were prepared by mixing the mother solutions in the target ratio. The perovskite precursor soloution was spin-coated on the PCBM substrate using the following parameters: 200 rpm for 2 seconds, 2000 rpm for 2 seconds, and 5000 rpm for 40 seconds (a=3 seconds). Then, 180 μL of chlorobenzene was dropped on the film at 20 seconds, followed by annealing at 110°C for 10 minutes and 150°C for 5 minutes. PDCBT as a hole transporting layer was spin-coated at 2000 rpm for 40 seconds and annealed at 90°C for 5 minutes. Finally, 100 μL of Ta-WOx was coated on PDCBT at 2000 rpm for 30 seconds and annealed at 75°C in ambient air. A 100-nm-

thick Au electrode was deposited through a shadow mask *via* thermal evaporation. For the devices used in the stability tests, a 200 nm Au layer was deposited.

Device characterization: The *J-V* curves of the solar cells were obtained using a Keithley source under 100 mW cm^{-2} AM1.5G illumination. The *J-V* characteristics were measured from -0.1 to 1.2 V (forward scan) at a scan rate of 20 mV/s. No hysteresis is observed in the devices. For the thermal stability test at 85 °C/85%RH, the devices were stored in a sample box in a climate chamber in the dark without any encapsulation. The devices were tested before and after storing in the climate chamber for 50 hours. For the photo-stability test at 85 °C, the devices were stored in a sealed chamber with N_2 flow under metal halide light illumination (100 mW cm^{-2}). The devices were continueously measured with forward scan at a scan rate of 20 mV/s.

Acknowledgments

The authors thank members of MIT Photovoltaics Research Laboratory, in particularly Jim Serdy for setting up and maintaining the environmental chamber for accelerated aging tests; Antonio Buscemi and Isaac Metcalf for assistance in XRD measurements, Isaac Siyu Tian for initial image processing, and Shreyaa Raghavan for the user-friendly Python package development. SS thanks Dr. Masafumi Fukuto and Dr. Kevin Yager from Brookhaven National Laboratory for beamtime assistance. High-throughput GIWAXS images were collected at BM-11, NSLS-II. The authors thank Prof. Joshua Schrier (Fordham university) for the discussion on perovskite material discovery using machine learning techniques. SS further thanks Felice Frankel for valuable insights on graphic visualization, and Mariela Castillo for early-stage project management.

This study is based upon work supported by the Defense Advanced Research Projects Agency (DARPA) under Contract No. HR001118C0036. Any opinions, findings and conclusions or recommendations expressed in this material are those of the authors and do not necessarily reflect the views of DARPA. SS, NTPH, TB thank TOTAL S.A., US National Science Foundation grant CBET-1605547, and the Skoltech NGP program. AT was supported by Alfred Kordelin Foundation and Svenska Tekniska Vetenskaps-akademien i Finland. FO and ZR were supported by the U.S. Department of Energy under Photovoltaic Research and Development program under Award DE-EE0007535, and Singapore through the Singapore Massachusetts Institute of

Technology (MIT) Alliance for Research and Technology's Low Energy Electronic Systems research program This research used computational resources sponsored by the DOE Office of Energy Efficiency and Renewable Energy and located at National Renewable Energy Laboratory. YZ, TH and CJB gratefully acknowledges the financial support through the "Aufbruch Bayern" initiative of the state of Bavaria (EnCN and "Solar Factory of the Future"), the Bavarian Initiative "Solar Technologies go Hybrid" (SolTech), "ELF-PV Design and development of solution processed functional materials for the next generations of PV technologies'' by the Bavarian State Government (No. 44-6521a/20/4) and the DFG, Projects No. 182849149 – SFB 953, IGK2495 and INST 90/1093/1. JJY and MB were supported by the Institute for Soldier Nanotechnology (ISN) grant W911NF-13-D-0001, the National Aeronautics and Space Administration (NASA) grant NNX16AM70H, and the Eni-MIT Alliance Solar Frontiers Center.

Author Contributions

SS and TB conceived the project. SS designed the experiments and led the laboratory and synchrotron-based measurements. AT developed colour and chamber environment calibration. AT and LZ processed the camera data. FO and JF designed the Bayesian optimisation algorithms and instability index, and FO, AT, and LZ wrote the Bayesian optimisation implementation. JT synthesized all thin-films samples supervised by SS. YZ fabricated the devices. JT and NTPH performed laboratory structural and morphological characterisation. JT, AT, NTPH performed the film degradation tests. AG performed DFT calculations. TH, YZ and IMP performed device degradation tests. FO, AT, LZ, and JF developed the incorporation of DFT into the Bayesian optimisation loop, and AT implemented the Gaussian process model and probability distribution on phase stability. AE built the automatic humidity control supervised by SS and AT. CB and AT developed the camera control program and visualized degradation data. CB performed optical characterisation supervised by SS. SS, JT, NTPH, and JJY performed structural characterisation using synchrotron radiation. RL assisted the measurements at beamline BM-11, NSLS-II. ZR performed the teacher-student model for DFT and non-DFT optimisation comparison. CJB, MB, VS, JF and TB supervised the project. SS, AT, FO, and TB wrote the manuscript with contributions from all co-authors. All authors discussed the results and inferred the implications of the project.

Declaration of Interests

Our laboratory has filed IP pertaining to various aspects of materials development. Authors declare no other competing interests.

References and Notes

[1] Boyd CC, Cheacharoen R, Leijtens T, McGehee MD. Understanding Degradation Mechanisms and Improving Stability of Perovskite Photovoltaics. Chem Rev 2019;119:3418–51. doi:10.1021/acs.chemrev.8b00336.

[2] Jeon NJ, Noh JH, Yang WS, Kim YC, Ryu S, Seo J, et al. Compositional engineering of perovskite materials for high-performance solar cells. Nature 2015;517:476–80. doi:10.1038/nature14133.

[3] Saliba M. Polyelemental, Multicomponent Perovskite Semiconductor Libraries through Combinatorial Screening. Adv Energy Mater 2019;9:1803754. doi:10.1002/aenm.201803754.

[4] Khenkin M V., Katz EA, Abate A, Bardizza G, Berry JJ, Brabec C, et al. Consensus statement for stability assessment and reporting for perovskite photovoltaics based on ISOS procedures. Nat Energy 2020;5:35–49. doi:10.1038/s41560-019-0529-5.

[5] Rohr B, Stein HS, Guevarra D, Wang Y, Haber JA, Aykol M, et al. Benchmarking the acceleration of materials discovery by sequential learning. Chem Sci 2020;11:2696–706. doi:10.1039/c9sc05999g.

[6] Zhang W, Mao J, Li S, Chen Z, Guo Z. Phosphorus-Based Alloy Materials for Advanced Potassium-Ion Battery Anode. J Am Chem Soc 2017;139:3316–9. doi:10.1021/jacs.6b12185.

[7] George EP, Raabe D, Ritchie RO. High-entropy alloys. Nat Rev Mater 2019;4:515–34. doi:10.1038/s41578-019-0121-4.

[8] Zhong M, Tran K, Min Y, Wang C, Wang Z, Dinh CT, et al. Accelerated discovery of CO2 electrocatalysts using active machine learning. Nature 2020;581:178–83. doi:10.1038/s41586-020-2242-8.

[9] Kumar G, Bossert H, McDonald D, Chatzidimitriou A, Ardagh MA, Pang Y, et al. Catalysis-in-a-Box: Robotic Screening of Catalytic Materials in the Time of COVID-19 and Beyond. Matter 2020;3:805–23. doi:10.1016/j.matt.2020.06.025.

[10] Burger B, Maffettone PM, Gusev V V., Aitchison CM, Bai Y, Wang X, et al. A mobile robotic chemist. Nature 2020;583:237–41. doi:10.1038/s41586-020-2442-2.

[11] Cole JM. A Design-to-Device Pipeline for Data-Driven Materials Discovery. Acc Chem Res 2020;53:599–610. doi:10.1021/acs.accounts.9b00470.

[12] Gómez-Bombarelli R, Aguilera-Iparraguirre J, Hirzel TD, Duvenaud D, Maclaurin D, Blood-Forsythe MA, et al. Design of efficient molecular organic light-emitting diodes by a high-throughput virtual screening and experimental approach. Nat Mater 2016;15:1120–7. doi:10.1038/nmat4717.

[13] Kirman J, Johnston A, Kuntz DA, Askerka M, Gao Y, Todorović P, et al. Machine-Learning-Accelerated Perovskite Crystallization. Matter 2020;2:938–47. doi:10.1016/j.matt.2020.02.012.

[14] Li Z, Najeeb MA, Alves L, Sherman A, Parrilla PC, Pendleton IM, et al. Robot-Accelerated Perovskite Investigation and Discovery (RAPID): 1. Inverse Temperature Crystallization 2019. doi:10.26434/CHEMRXIV.10013090.V1.

[15] MacLeod BP, Parlane FGL, Morrissey TD, Häse F, Roch LM, Dettelbach KE, et al. Self-driving laboratory for accelerated discovery of thin-film materials. Sci Adv 2020;6:eaaz8867. doi:10.1126/sciadv.aaz8867.

[16] Xue D, Balachandran P V., Yuan R, Hu T, Qian X, Dougherty ER, et al. Accelerated search for BaTiO3-based piezoelectrics with vertical morphotropic phase boundary using Bayesian learning. Proc Natl Acad Sci U S A 2016;113:13301–6. doi:10.1073/pnas.1607412113.

[17] Epps RW, Bowen MS, Volk AA, Abdel-Latif K, Han S, Reyes KG, et al. Artificial Chemist: An Autonomous Quantum Dot Synthesis Bot. Adv Mater 2020;32:2001626. doi:10.1002/adma.202001626.

[18] Gu E, Tang X, Langner S, Duchstein P, Zhao Y, Levchuk I, et al. Robot-Based High-Throughput Screening of Antisolvents for Lead Halide Perovskites. Joule 2020;4:1806–22. doi:10.1016/j.joule.2020.06.013.

[19] Higgins K, Valleti SM, Ziatdinov M, Kalinin S, Ahmadi M. Chemical Robotics Enabled Exploration of Stability and Photoluminescent Behavior in Multicomponent Hybrid Perovskites via Machine Learning 2020. doi:10.26434/CHEMRXIV.12436079.V1.

[20] Choubisa H, Askerka M, Ryczko K, Voznyy O, Mills K, Tamblyn I, et al. Crystal Site Feature Embedding Enables Exploration of Large Chemical Spaces. Matter 2020;3:433–48. doi:10.1016/j.matt.2020.04.016.

[21] Curtarolo S, Hart GLW, Nardelli MB, Mingo N, Sanvito S, Levy O. The High-throughput Highway to Computational Materials Design. Nat Mater 2013;12:191–201. doi:10.1038/nmat3568.

[22] Jesper Jacobsson T, Correa-Baena J-P, Pazoki M, Saliba M, Schenk K, Grätzel M, et al. Exploration of the compositional space for mixed lead halogen perovskites for high efficiency solar cells. Energy Environ Sci 2016;9:1706–24. doi:10.1039/C6EE00030D.

[23] Schelhas LT, Li Z, Christians JA, Goyal A, Kairys P, Harvey SP, et al. Insights into operational stability and processing of halide perovskite active layers. Energy Environ Sci 2019;12:1341–8. doi:10.1039/c8ee03051k.

[24] SheffieldML/GPyOpt: Gaussian Process Optimization using GPy n.d. https://github.com/SheffieldML/GPyOpt (accessed July 1, 2020).

[25] Zhu XH, Wei ZR, Jin YR, Xiang AP. Growth and characterization of a PbI2 single crystal used for gamma ray detectors. Cryst Res Technol 2007;42:456–9. doi:10.1002/crat.200610847.

[26] Hu Y, Bai F, Liu X, Ji Q, Miao X, Qiu T, et al. Bismuth Incorporation Stabilized α-CsPbI3 for Fully Inorganic Perovskite Solar Cells. ACS Energy Lett 2017;2:2219–27. doi:10.1021/acsenergylett.7b00508.

[27] Masi S, Echeverría-Arrondo C, Salim KMM, Ngo TT, Mendez PF, López-Fraguas E, et al. Chemi-Structural Stabilization of Formamidinium Lead Iodide Perovskite by Using Embedded Quantum Dots. ACS Energy Lett 2020:418–27. doi:10.1021/acsenergylett.9b02450.

[28] Hashmi SG, Tiihonen A, Martineau D, Ozkan M, Vivo P, Kaunisto K, et al. Long term stability of air processed inkjet infiltrated carbon-based printed perovskite solar cells under intense ultra-violet light soaking. J Mater Chem A 2017;5:4797–802. doi:10.1039/c6ta10605f.

[29] Hashmi SG, Martineau D, Li X, Ozkan M, Tiihonen A, Dar MI, et al. Air Processed Inkjet Infiltrated Carbon Based Printed Perovskite Solar Cells with High Stability and Reproducibility. Adv Mater Technol 2017;2:1600183. doi:10.1002/admt.201600183.

[30] Stoddard RJ, Dunlap-Shohl WA, Qiao H, Meng Y, Kau WF, Hillhouse HW. Forecasting the Decay of Hybrid Perovskite Performance Using Optical Transmittance or Reflected Dark-Field Imaging. ACS Energy Lett 2020;5:946–54. doi:10.1021/acsenergylett.0c00164.

[31] Kim S, Eom T, Ha Y-S, Hong K-H, Kim H. Thermodynamics of Multicomponent Perovskites: A Guide to Highly Efficient and Stable Solar Cell Materials. Chem Mater 2020;32:4265–72. doi:10.1021/acs.chemmater.0c00893.

[32] Knight AJ, Herz LM. Preventing phase segregation in mixed-halide perovskites: a perspective. Energy Environ Sci 2020. doi:10.1039/d0ee00788a.

[33] Herbol HC, Poloczek M, Clancy P. Cost-effective materials discovery: Bayesian optimization across multiple information sources. Mater Horizons 2020. doi:10.1039/D0MH00062K.

[34] Doan HA, Agarwal G, Qian H, Counihan MJ, Rodríguez-López J, Moore JS, et al. Quantum Chemistry-Informed Active Learning to Accelerate the Design and Discovery of Sustainable Energy Storage Materials. Chem Mater 2020. doi:10.1021/acs.chemmater.0c00768.

[35] Gelbart MA, Snoek J, Adams RP. Bayesian optimization with unknown constraints. Uncertain. Artif. Intell. - Proc. 30th Conf. UAI 2014, 2014, p. 250–9.

[36] Saliba M, Matsui T, Seo J-Y, Domanski K, Correa-Baena J-P, Nazeeruddin MK, et al. Cesium-containing triple cation perovskite solar cells: improved stability, reproducibility and high efficiency. Energy Environ Sci 2016;9:1989–97. doi:10.1039/C5EE03874J.

[37] Kieslich G, Sun S, Cheetham AK. Solid-state principles applied to organic–inorganic perovskites: new tricks for an old dog. Chem Sci 2014;5:4712–5.

doi:10.1039/C4SC02211D.

[38] Li Z, Yang M, Park J-S, Wei S-H, Berry JJ, Zhu K. Stabilizing Perovskite Structures by Tuning Tolerance Factor: Formation of Formamidinium and Cesium Lead Iodide Solid-State Alloys. Chem Mater 2016;28:284–92. doi:10.1021/acs.chemmater.5b04107.

[39] Correa-Baena JP, Saliba M, Buonassisi T, Grätzel M, Abate A, Tress W, et al. Promises and challenges of perovskite solar cells. Science 2017;358:739–44. doi:10.1126/science.aam6323.

[40] Saidaminov MI, Williams K, Wei M, Johnston A, Quintero-Bermudez R, Vafaie M, et al. Multi-cation perovskites prevent carrier reflection from grain surfaces. Nat Mater 2020;19:412–8. doi:10.1038/s41563-019-0602-2.

[41] Correa-Baena J-P, Luo Y, Brenner TM, Snaider J, Sun S, Li X, et al. Homogenized Halides and Alkali Cation Segregation in Alloyed Organic-inorganic Perovskites. Science 2019;363:627–31. doi:10.1126/science.aah5065.

[42] González J, Dai Z, Hennig P, Lawrence N. Batch Bayesian Optimization via Local Penalization. n.d.

[43] Goodfellow I, Bengio Y, Courville A. Deep Learning. MIT press Cambridge; 2016.

[44] Goyal A, McKechnie S, Pashov D, Tumas W, Schilfgaarde M van, Stevanović V. Origin of Pronounced Nonlinear Band Gap Behavior in Lead–Tin Hybrid Perovskite Alloys. Chem Mater 2018;30:3920–8. doi:10.1021/acs.chemmater.8b01695.

[45] Blöchl PE. Projector augmented-wave method. Phys Rev B 1994;50:17953–79. doi:10.1103/PhysRevB.50.17953.

[46] Kresse G, Furthmüller J. Efficiency of ab-initio total energy calculations for metals and semiconductors using a plane-wave basis set. Comput Mater Sci 1996;6:15–50. doi:10.1016/0927-0256(96)00008-0.

[47] Perdew JP, Burke K, Ernzerhof M. Generalized gradient approximation made simple. Phys Rev Lett 1996;77:3865–8. doi:10.1103/PhysRevLett.77.3865.

[48] Monkhorst HJ, Pack JD. Special points for Brillouin-zon integrations. Phys Rev B 1976;13:5188–92. doi:10.1103/PhysRevB.16.1748.

[49] Stoumpos CC, Malliakas CD, Kanatzidis MG. Semiconducting Tin and Lead Iodide Perovskites with Organic Cations: Phase Transitions, High Mobilities, and Near-infrared Photoluminescent Properties. Inorg Chem 2013;52:9019–38. doi:10.1021/ic401215x.

[50] Zunger A, Wei SH, Ferreira LG, Bernard JE. Special quasirandom structures. Phys Rev Lett 1990;65:353–6. doi:10.1103/PhysRevLett.65.353.

[51] Van de Walle A, Asta M, Ceder G. The alloy theoretic automated toolkit: A user guide. Calphad Comput Coupling Phase Diagrams Thermochem 2002;26:539–53. doi:10.1016/S0364-5916(02)80006-2.

[52] Van De Walle A, Tiwary P, De Jong M, Olmsted DL, Asta M, Dick A, et al. Efficient stochastic generation of special quasirandom structures. Calphad Comput Coupling Phase

Diagrams Thermochem 2013;42:13–8. doi:10.1016/j.calphad.2013.06.006.

[53] Lejaeghere K, Bihlmayer G, Björkman T, Blaha P, Blügel S, Blum V, et al. Reproducibility in density functional theory calculations of solids. Science 2016;351. doi:10.1126/science.aad3000.

[54] https://github.com/CFN-softbio/SciAnalysis n.d.

Figure and scheme titles and legends

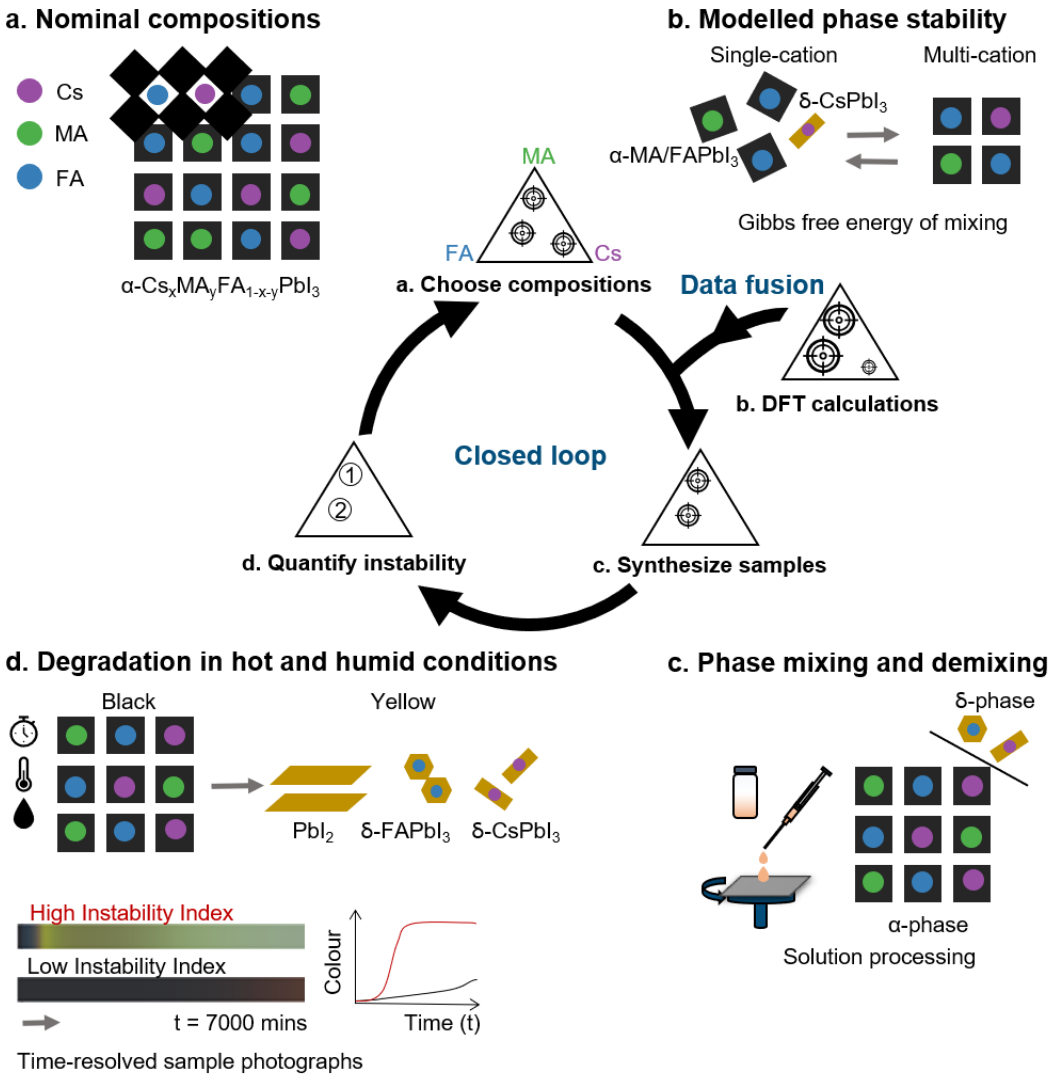

Figure 1 Each optimisation round consists of three steps of 'composition selection', 'film synthesis', and 'instability quantification' and a fourth step of theoretical incorporation into the closed-loop

workflow by a data fusion approach. **a**. Composition selection: the selection of nominal compositions of multi-cation perovskites is driven by machine learning algorithms. b. Data fusion: DFT-modelled ΔG_{mix} is incorporated in the optimization algorithm as a constraint. **c**. Film synthesis: tuning A-site cations in lead iodide perovskites forms $Cs_xMA_yFA_{1-x-y}PbI_3$, a space of 5151 compositions (estimated experimental resolution 1%). Thin-film samples are spin-coated in series using precursor solutions of nominal compositions. **d**. Instability quantification: we perform accelerated high-throughput degradation tests with *in situ* optical monitoring, enabling 28 thin-film samples being degraded in parallel. Near-black photoactive perovskite films turn yellow over time due to the emergence of high-bandgap degradation products. Quantified optical changes over time, recorded in R (red), G (green), and B (blue) channels, are used as a proxy to evaluate the chemical instability of the samples under 85% relative humidity (RH), 85°C sample temperature, and 0.15 Sun visible only illumination. Two representative sets of sample photographs and curves of the total (R + G + B) area-averaged value as a function of time are illustrated in d.

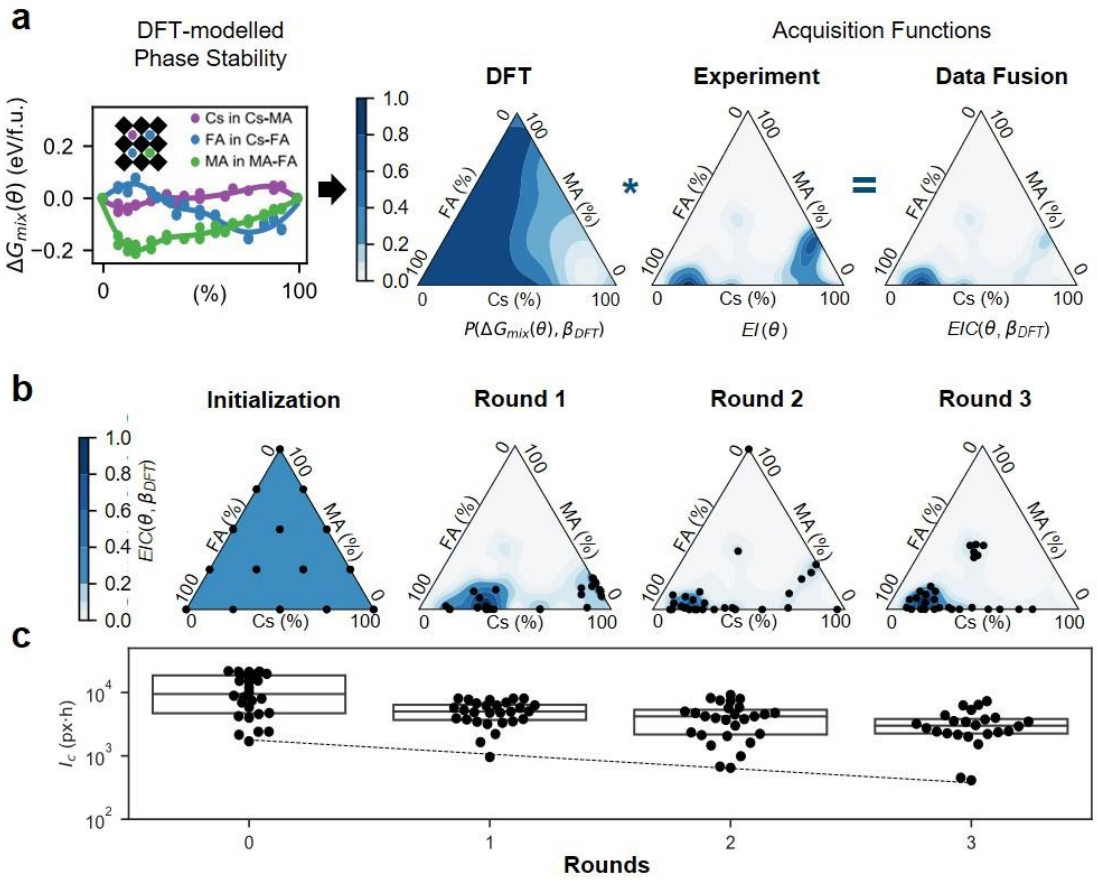

Figure 2 Fusion of DFT and experiments guides the optimisation of compositional stability. **a**. DFT-modelled Gibbs free energy of mixing, ΔG_{mix}, of 47 binary compositions of CsMA, CsFA, and MAFA α-perovskites relative to end members of δ-$CsPbI_3$, α-$MAPbI_3$, and α-$FAPbI_3$. We fit a Gibbs free-energy

model, $\Delta G_{mix}(\Theta)$, where Θ is a composition in the ternary space, to the phase thermodynamics data using Gaussian process regression. $\Delta G_{mix}(\Theta)$ is transformed into a probabilistic constraint, $P(\Delta G_{mix}(\Theta), \beta_{DFT})$ that models the cumulative probability of phase mixing at above 300K. Multiplying *P* with the acquisition function of the Bayesian optimisation algorithm, $EI(\Theta)$, gives a DFT-weighted acquisition function, $EIC(\Theta)$. **b**. Starting from equally-spaced 15 compositions in the initialization round, in each optimisation round, 28 sample films (black markers) are synthesized and undergo degradation tests. Compositions are chosen by Bayesian optimisation algorithm that suggests them using $EIC(\Theta)$ (blue surface colour). **c**. Experimentally measured *Instability Indices*, I_c (pixels*hours), of 112 samples over one initialisation and three optimisation rounds. The black boxes indicate the mean and standard deviation of each round. The dashed line indicating the most stable compositions in each experimental round is for eye guidance only.

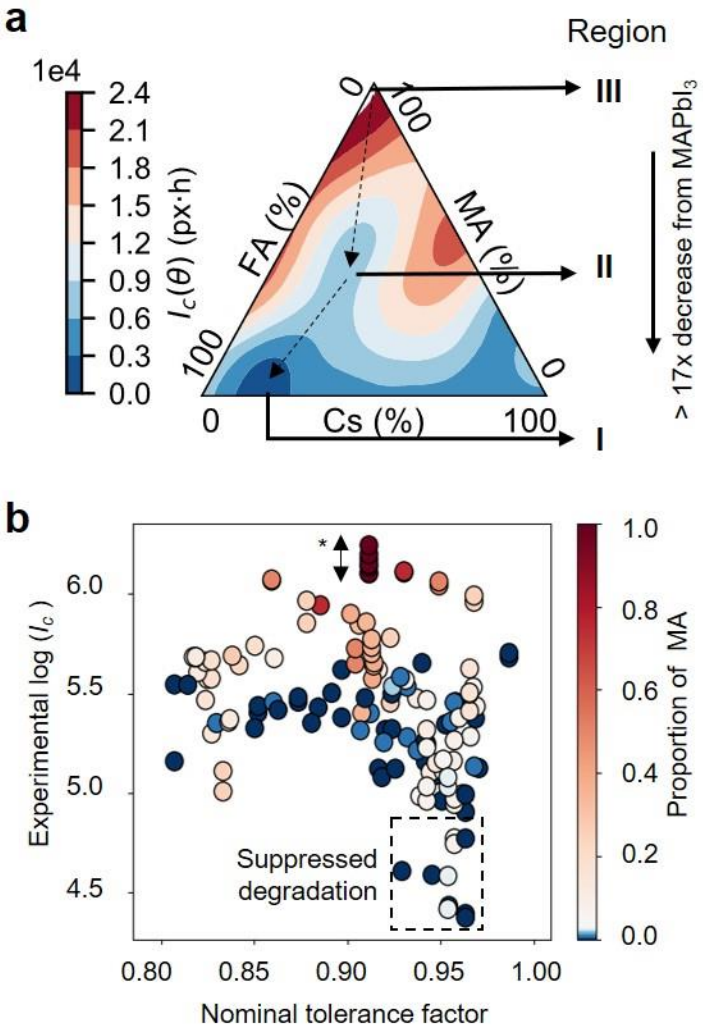

Figure 3 Composition-dependent instability landscape. **a**. The instability landscape $I_c(\Theta)$ mapped over the $Cs_xMA_yFA_{1-x-y}PbI_3$ compositional space evolves in time. The posterior mean of the Bayesian

optimisation surrogate model estimating I_c is shown after 6h at the end of the aging test (using the experimentally measured samples from Round 0-3). Three distinct compositional regions are identified. Regions I-III are labelled following ascending order of measured I_c. **b.** Roles of cations in the realised degradation routes. a. I_c of all experimentally measured samples as a function of Goldschmidt's tolerance factor, co-visualizing the proportion of MA. *Experimental uncertainty of measured I_c across batches in the control composition, $MAPbI_3$ (see Supplemental Data for full list of samples).

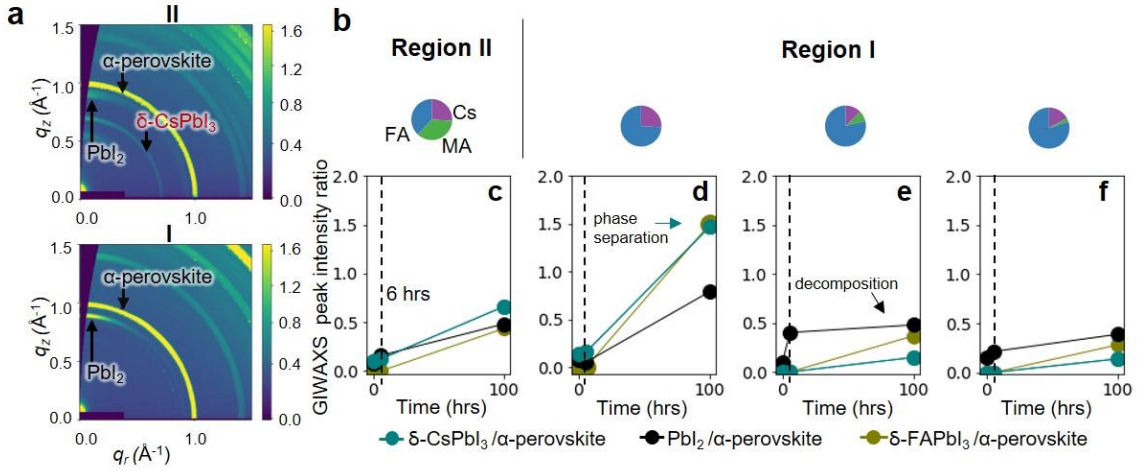

Figure 4 Degradation mechanisms in optimized perovskites. **a.** GIWAXS images of the as-synthesized thin-films of $Cs_{0.26}MA_{0.36}FA_{0.38}PbI_3$ in Region II and the ML-optimum composition, $Cs_{0.17}MA_{0.03}FA_{0.80}PbI_3$, in Region I. Over-stoichiometric precursors with excess PbI_2 were added in all samples following the high-efficiency perovskite solar cell recipe in ref. [36] **b.** GIWAXS peak intensity ratios of the non-perovskite phases and PbI_2 relative to the perovskite phase as an estimate for the extent of degradation for representative compositions in Region I and II, including **c**. $Cs_{0.26}MA_{0.36}FA_{0.38}PbI_3$ in Region II, **d**. $Cs_{0.26}FA_{0.74}PbI_3$ near the boundary of Region I and II with high Cs , **e**. $Cs_{0.13}MA_{0.08}FA_{0.79}PbI_3$ near the boundary of Region I and II with high MA, and **f**. $Cs_{0.17}MA_{0.03}FA_{0.8}PbI_3$ at the center of Region I.

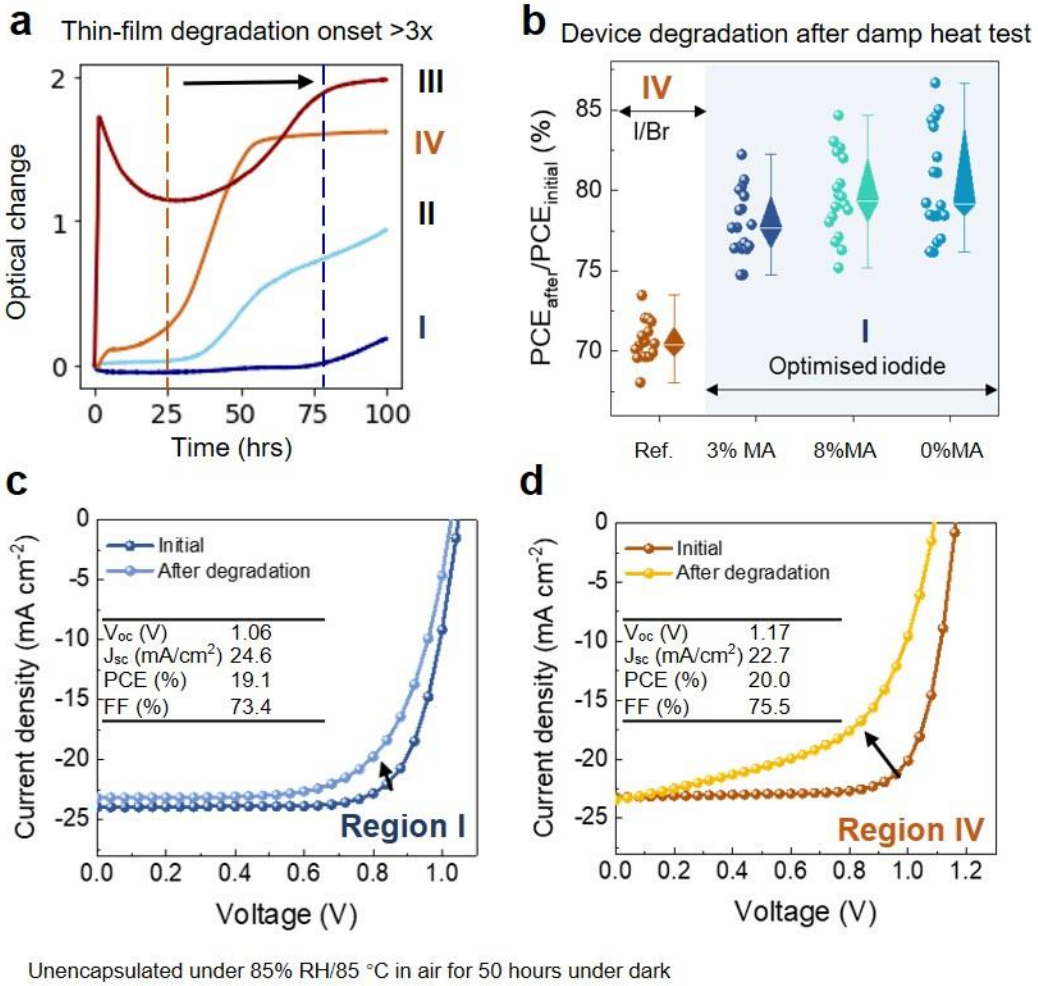

Figure 5 Suppressed degradation in thin-film and photovoltaic devices. **a**. Optical changes as a function of degradation time, showing the onset of degradation for representative compositions in regions I-IV, $Cs_{0.17}MA_{0.03}FA_{0.80}PbI_3$, $Cs_{0.26}MA_{0.36}FA_{0.38}PbI_3$, $Cs_{0.05}(MA_{0.17}FA_{0.83})_{0.95}Pb(I_{0.83}Br_{0.17})_3$ (I/Br), and $MAPbI_3$ respectively. **b**. The percentage ratios of the solar cell efficiency after 50 hours' full damp heat degradation tests for unencapsulated devices over the initial efficiencies based on I/Br and three ML-informed compositions in Region I, $Cs_{0.17}MA_{0.03}FA_{0.80}PbI_3$, $Cs_{0.13}MA_{0.08}FA_{0.79}PbI_3$, and $Cs_{0.13}FA_{0.87}PbI_3$ respectively. **c**. Initial device efficiency based on the ML-optimum composition in Region I, and the their current-voltage curves before and after 50 hours' accelerated degradation tests under 85% RH/85°C unencapsulated in air in dark. **d.** Initial device efficiency based on the I/Br reference composition in Region IV, and the their current-voltage curves before and after the same degradation tests as in c.

Supplemental Information

Supplemental Experimental Procedures, Figures S1-S19, Tables S1-S6.

Supplemental Video S1: Optical changes of perovskite thin-films in initialization Round 0, and Supplemental Video S2: Optical changes of perovskite thin-films in optimization Round 3.

Supplemental Data S1: Synthetic parameters, structural stability data, modelling parameters, uncertainty quantification in Round 0, and results of grazing incidence X-ray diffraction.